



# High-resolution ionospheric observations and modeling over Belgium during the solar eclipse of 20 March 2015 including first results of ionospheric tilt and plasma drift measurements

Tobias G.W. Verhulst<sup>\*</sup>, Danislav Sapundjiev, Stanimir M. Stankov<sup>\*</sup>

*Royal Meteorological Institute (RMI), Ringlaan 3, B-1180 Brussels, Belgium*

Received 19 January 2016; received in revised form 4 March 2016; accepted 6 March 2016

Available online 11 March 2016

## Abstract

The ionospheric behavior over Belgium during the partial solar eclipse of 20 March 2015 is analyzed based on high-resolution solar radio flux, vertical incidence sounding, and GPS *TEC* measurements. First results of ionosonde-based ionospheric plasma drift and tilt observations are presented and analyzed, including some traveling ionospheric disturbances caused by the eclipse. Also, collocated ionosonde and GPS measurements are used to reconstruct the time evolution of the vertical electron density distribution using the Royal Meteorological Institute (RMI) ionospheric specification system, called Local Ionospheric Electron Density profile Reconstruction (LIEDR).

© 2016 COSPAR. Published by Elsevier Ltd. All rights reserved.

*Keywords:* Solar eclipse; Traveling ionospheric disturbances; Ionospheric drift and tilt; Ionosonde; Digisonde

## 1. Introduction

Solar eclipses have long since attracted attention with the relatively rare conditions they create and, thus, the opportunities they offer for ionospheric research (Beynon and Brown, 1956). It was soon recognized that the eclipses can be particularly useful when studying the solar ionizing radiation and various effects on both the thermosphere and the ionosphere, including temperature balance, production and loss in the lower ionosphere, transport processes in the upper ionosphere, etc. (Rishbeth, 1968, 1970).

One might be tempted to think that (total) eclipse conditions can be considered the same as the night conditions, albeit short-lived. However, since the space shadowed by the Moon's passage in front of the Sun is relatively small, the decay rate of the ionosphere is not the same as during

night because of the compensating effect of the ionization coming from the adjacent (sunlit) regions. This, and the fact that different eclipses occur at different locations and seasons, makes the eclipse studies quite difficult actually.

Earlier investigations of eclipse effects on the ionosphere were carried out by observing the changes in intensity of radio waves reflected from the ionosphere, followed by absorption measurements at oblique incidence on one or several frequencies (Beynon and Brown, 1956, and references therein), vertical incidence sounding (VIS) with ionosondes (Nestorov and Taubenheim, 1962), in situ measurements with rockets and satellites, total electron content (*TEC*) deduced by observing the Faraday rotation of polarization of lunar radio waves (Klobuchar and Whitney, 1965), incoherent scatter radar measurements of plasma density, temperature and drifts (Baron and Hunsucker, 1973), and – with the advancement of the Global Positioning System (GPS) technology – via GPS-based *TEC* observations (Afraimovich et al., 1998; Rashid et al.,

<sup>\*</sup> Corresponding authors.

*E-mail address:* [tobias.verhulst@oma.be](mailto:tobias.verhulst@oma.be) (T.G.W. Verhulst).

2006). Simultaneous multi-instrument observations (at single and/or several locations) (Farges et al., 2001; Jakowski et al., 2008; Le et al., 2009; Chuo, 2013; Kumar et al., 2013) together with targeted modeling studies (Müller-Wodarg et al., 1998; Korenkov et al., 2002) seems to be the most efficient way of studying the complex, multifaceted nature of solar eclipses and their effects on the ionosphere.

While, initially, the efforts went on investigating the source of atmospheric ionization (electromagnetic or corpuscular radiation) and the chemical composition of the upper atmosphere (e.g. ionospheric plasma recombination rates), the interest shifted in recent years towards investigating the atmospheric gravity wave (AGW) phenomena generated by the Moon's shadow passing (at a supersonic speed) through the atmosphere (Chimonas and Hines, 1970; Davis et al., 2001; Altadill et al., 2001; Jakowski et al., 2008).

An eclipse affects all ionospheric layers although with different strength and manifestation of the effects. At lower altitudes (in the ionospheric *D* and *E* layers), the amount of ionization is governed by ion production and loss processes (photochemical equilibrium) while at higher altitudes the drift (transport) processes take precedence.

The presence of (substantial) ionospheric tilt and plasma drifts impedes the accuracy (and, in some cases, even the implementation) of some of the above-mentioned observation techniques. It is therefore important to have these (tilt and drift) measurements carried out in parallel to other measurements and considered when studying the eclipse effects.

A total solar eclipse occurred on 20 March 2015 with most of the total eclipse path located in the North Atlantic (Fig. 1). As a result, a partial solar eclipse was visible from Belgium on the same day between 8:27 UT (start,  $t_s$ ) and 10:47 UT (end,  $t_e$ ), with a maximum eclipse of 81.5% recorded at 09:34 UT (max,  $t_m$ ).

The paper presents first results and analyses of ionosonde-based ionospheric plasma drift and tilt observations together with a reconstruction of the local vertical plasma redistribution in an unprecedented high-cadence survey.

## 2. Instrumentation and measurements

Spectral radio observations of the Sun are carried out by the Royal Observatory of Belgium (ROB) in Humain (50.2°N, 5.2°E). The Humain Radio-Astronomy Station (RAS) employs a radio telescope consisting of a 6-m Sun-tracking parabola with a receiver antenna placed at the focus. The instrument measures the solar radio flux (SRF) with a sampling rate of 250 ms (integrated over 6-s time periods) at pre-selected frequencies, delivering valuable information about the solar irradiance and flares.

A high-performance NovAtel GPStation-6™ is used to provide 1-s Total Electron Content (*TEC*) measurements. The receiver can track all present and upcoming Global Navigation Satellite System (GNSS) constellations and

satellite signals with a maximum sampling rate of 50 Hz for each of the 120 available tracking channels.

The principal instrument used in this study is the Digisonde-4D® (Reinisch et al., 2009), installed at the RMI Geophysical Center in Dourbes (50.1°N, 4.6°E). Digisonde-4D is a state-of-the-art equipment using radar principles of remote sensing to evaluate with high-accuracy and precision the conditions of the ionospheric plasma above the station. It boasts multiple functionalities supported by a fully automated operational and database management system. It is capable of simultaneously measuring the following observables reflected (in vertical incidence) or refracted (in oblique incidence) signals from the ionosphere: frequency, range, amplitude, phase, Doppler shift and spread, angle of arrival, and wave polarization. Signal transmission is performed with two (NE-SW and NW-SE) crossed “delta” antennas of 40 m in height and reception is done with an array of four crossed magnetic dipole receive antennas in a triangular arrangement. The Digisonde is equipped with the latest versions of the computer software for automatic ionogram interpretation, ARTIST-5 (Galkin and Reinisch, 2008), and Digisonde Drift Analysis, DDA (Kozlov and Paznukhov, 2008). For the purpose of this study, the Digisonde was used to produce ionogram and drift measurements with a time resolution of 30 s. Some of the Digisonde operational settings for the eclipse campaign are listed in Table 1.

The measurements during the eclipse on 20 March 2015 were compared with the same type of measurements from a “control” (or “reference”) day, 21 March 2015, when the geophysical conditions were back to normal. The sampling rate was kept unchanged during both the eclipse and control days.

## 3. Solar radio flux observations

The Humain RAS recorded the solar radio flux (Fig. 2) during the eclipse as the Moon was moving in front of the Sun and, again, during the same period on the control day. During the eclipse, the solar flux decreased steadily from about 08:30 UT to a minimum at about 09:30 UT before recovering to its pre-eclipse values at about 11:00 UT. The spikes on the frequency curves are caused by solar bursts (when appearing simultaneously on different curves) or by interference. Ripples are due to interference with the telescope parabola reception by the solar radiation reflected from the ground.

## 4. GPS-based observations of the vertical TEC

Fig. 3 shows the vertical *TEC* for the eclipse and reference days at 60-s time resolution. Similar to the critical frequency ( $f_oF_2$ , see Section 5), the reference-day *TEC* shows a straightforward linear increase, expected for this time of day. During the eclipse, *TEC* behaves similarly to  $f_oF_2$ : around 08:00 UT it starts to deviate from the reference,

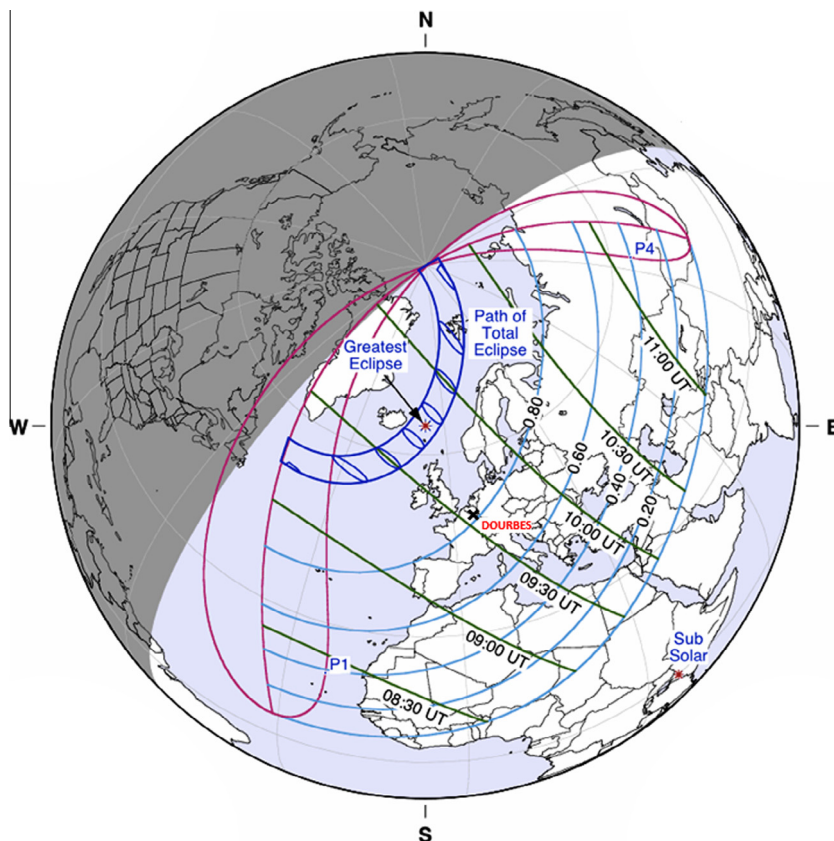


Fig. 1. Schematic map of the 20 March 2015 solar eclipse path (Eclipse Predictions by Fred Espenak, NASA/GSFC).

Table 1  
Digisonde settings during the March 2015 eclipse campaign in Dourbes.

	Ionogram	SkyMap
Frequencies	1–10 MHz Coarse step 25 kHz	5 MHz Five 50 kHz fine steps
Polarity	O only	O only
Integrated repeats	4	128
Wave form	66.6 $\mu$ s Pulse	16-Chip complementary
Starting seconds	00 & 30	15 & 45
Sounding time	14.470 s	12.830 s

stagnating around 12–14 TECU (1 TECU =  $10^{16}$  el/m<sup>2</sup>) before starting to decrease when the eclipse reaches its maximum. This is in good agreement with the observations of the 11 August 1999 (Bamford, 2001) and 3 October 2005 eclipses over Europe (Jakowski et al., 2008).

### 5. Vertical incidence sounding observations of key ionospheric layers characteristics

For a more reliable comparison with previous eclipse studies, presented also here are the variations of key ionospheric characteristics such as the *E*-layer critical frequency ( $f_oE$ ) (Fig. 4), the *F*-layer critical frequency ( $f_oF_2$ ) (Fig. 5), and the *F*-layer peak density height ( $h_mF_2$ ) (Fig. 6), for both the day of the eclipse and the reference day. These characteristics were automatically scaled by the ARTIST-5 software.

Since the *E* layer is a daytime phenomenon, maintained mostly by photoionization of neutral components of the atmosphere, it is expected to react promptly to the lack (or decrease) of solar irradiation. Indeed, shortly after the start of the eclipse,  $f_oE$  started to decrease from its normal-day values of about 2.8 MHz at 08:30 UT down to 2.5 MHz about 15 min later. The values remained low until about 10:45 UT when the frequency started to increase steadily up to their normal values reached shortly before the end of the eclipse.

Given the increased difficulty of automatically scaling the measured parameters due to the increased rate of sounding (cf. Table 1), the autoscaling software did remarkably well in identifying the correct  $f_oF_2$  values. Visual inspection makes it immediately clear which points are outliers that can be discarded and what the real behavior of  $f_oF_2$  is. The divergence from the normal (quiet-time) diurnal evolution of  $f_oF_2$  during the eclipse is clear: the usual morning-time increase is interrupted after 06:30 UT and, from around 07:45 UT until 09:15 UT, a plateau is formed with  $f_oF_2$  stagnating around 5.0 MHz, followed by a steep decrease down to 4.1 MHz at 09:45 UT, before starting to climb again. Note that the values of the critical frequency,  $f_oF_2$ , on the day of the eclipse start to deviate from their averages (and from those on the reference day) even before the eclipse has started over Belgium at  $t_s$ . This can be explained by plasma moving towards the

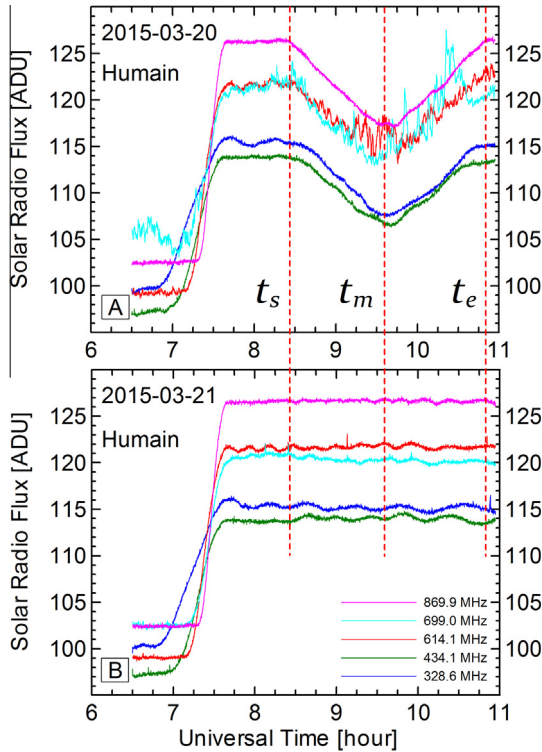


Fig. 2. Solar radio flux (in Analog–Digital Units) measured in Humain on the eclipse day, 20 March 2015 (panel A), and on a normal day, 21 March 2015 (panel B), at five selected frequencies ranging from 328.6 MHz to 869.9 MHz. On March 20, frequencies 699.0 MHz and 614.1 MHz are affected by strong interferences, but the curves still follow the general trend of the other frequencies. Credit: Royal Observatory of Belgium (ROB).

region where the eclipse was already in progress at that time (the eclipse started over the Atlantic Ocean at 07:41 UT). However, we will discuss this observation after we assess the other (types of) measurements.

The  $E$ -layer peak height ( $h_m E$ ) is a very stable characteristic that remained unaffected by the eclipse and maintained its normal values of around 100 km (figure not shown).

The  $F$ -layer peak height,  $h_m F_2$  (Fig. 6), varied substantially during the eclipse although its automatic scaling was clearly not as good as that of  $f_o F_2$ . The latter was to be expected considering that the sunrise period, with the rapid changes in the ionosphere, is the most difficult period for autoscaling (Stankov et al., 2012), especially when such challenging ionosonde settings were used throughout this campaign. Nevertheless, one important feature of  $h_m F_2$ , observed between 09:45 UT and 10:15 UT (Fig. 6A), was its sudden increase opposite to the pronounced decrease in the critical frequency  $f_o F_2$  (Fig. 5A) during the same period.

## 6. Modeling the vertical ionospheric plasma distribution

For eclipse observations to be successfully used in ionospheric studies, detailed electron density profiling is a

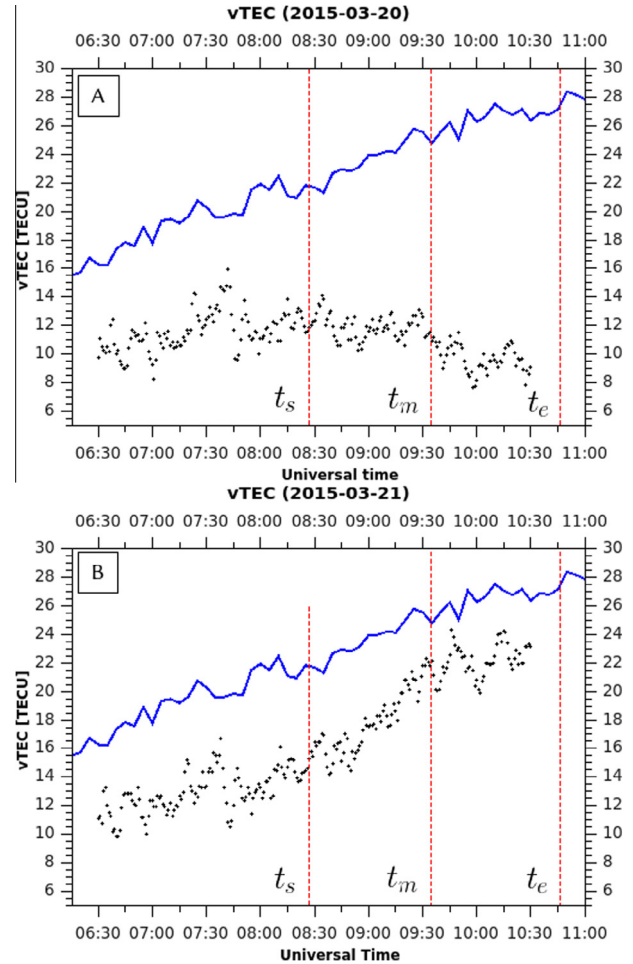


Fig. 3. Vertical  $TEC$  during the eclipse (panel A, crosses) and during the same period on the regular day (panel B, crosses). Instead of continuously increasing, which is the normal morning behavior, the  $TEC$  stagnates at 12–14 TECU before starting to gradually decrease after 08:30 UT. The solid curve represents the median behavior calculated from measurements of the 27-day period centered on the day of the eclipse.

necessity. Ionospheric characteristics scaled automatically from the ionograms together with the vertical  $TEC$  values calculated from the GNSS measurements are used here as input for the RMI Local Ionospheric Electron Density Reconstruction (LIEDR) system (Stankov et al., 2011). LIEDR uses  $f_o F_2$ ,  $f_o E$ ,  $M(3000)F_2$  and  $TEC$  as input parameters, as well as solar radio flux and geomagnetic measurements. It acquires and processes in real time the concurrent and collocated ionosonde and GNSS  $TEC$  measurements, and ultimately, deduces a full-height electron density profile based on a reconstruction technique (Stankov and Muhtarov, 2001; Stankov, 2002; Stankov et al., 2003) utilizing different ionospheric profilers (Exponential, Epstein, Chapman) and empirically-modeled values of the  $O^+ - H^+$  ion transition height. In this way, the topside profile is more adequately represented because of the use of independent additional information about the topside ionosphere. The retrieval of the electron density distribution is performed in two main stages: construction of the bottomside electron profile (below  $h_m F_2$ ) and construction of the

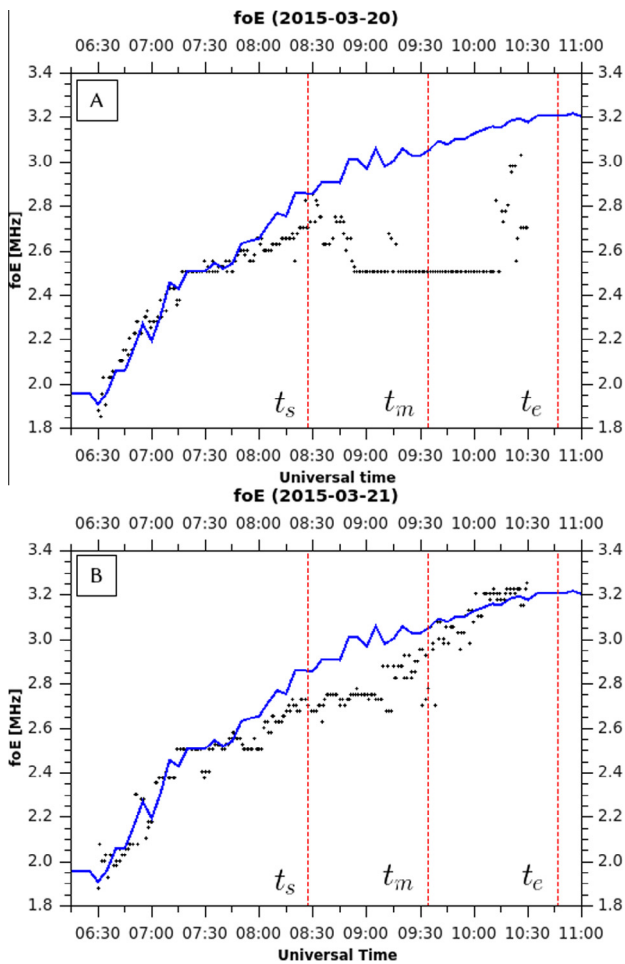


Fig. 4. The variation of the ionospheric E-layer critical frequency,  $f_oE$ , during the eclipse (panel A, crosses) and the control day (panel B, crosses). The solid curve represents the median behavior calculated from measurements of the 27-day period centered on the day of the eclipse.

topside profiles (above  $h_mF_2$ ). The ionosonde measurements are used for directly obtaining the lower part of the electron density profile. The corresponding bottomside part of  $TEC$  is calculated from this profile and is then subtracted from the entire  $TEC$  in order to obtain the unknown portion of  $TEC$  in the upper part. The topside  $TEC$  is used in the next stage for deducing the topside ion and electron profiles. The result is a full-height profile of the electron density distribution, from 90 km up to about 1100 km, which can be easily put on display (profilogram) for a close-up analysis (Fig. 7).

On both the eclipse and reference days, the LIEDR system was run for a first time at a 60-s time resolution, which is the resolution at which  $TEC$  values are available. The higher the sounding rate, the more accurately the changes in the ionosphere can be estimated (Bamford, 2001; Davis et al., 2001). In our study, the ionospheric characteristics are available at twice this rate (i.e. every 30 s), allowing for the implementation of a simple data cleaning procedure replacing the outliers with interpolated values.

A clear decrease in the ionization level is visible (Fig. 7) as a result of the decrease in the production rate. However,

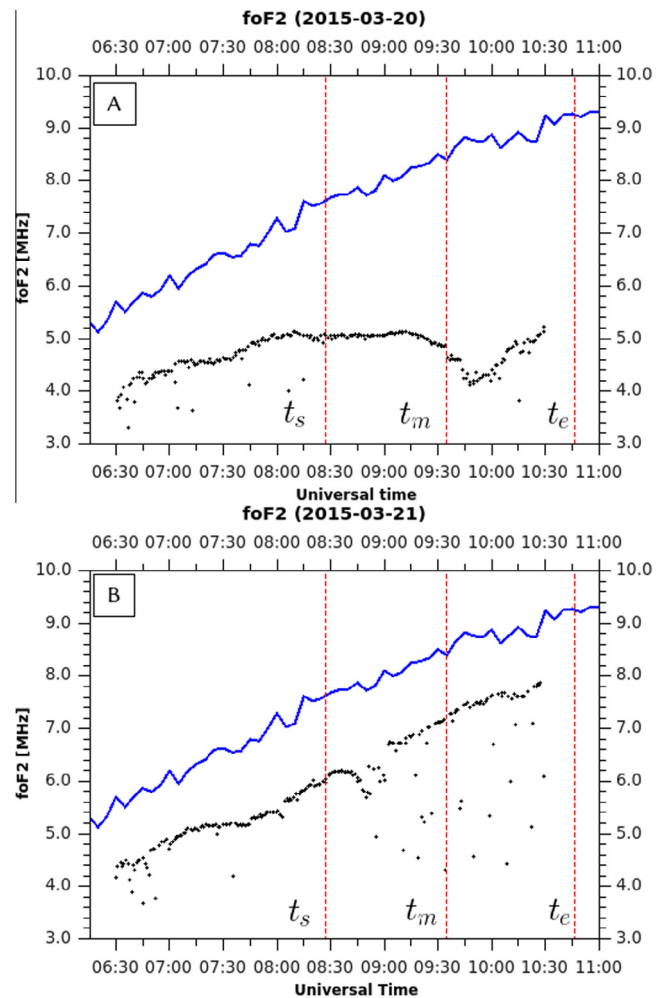


Fig. 5. Ionospheric F-layer critical frequency,  $f_oF_2$ , during the eclipse (panel A, crosses) and the control day (panel B, crosses). On the control day,  $f_oF_2$  exhibits the normal, quiet-time increase in the morning. On the day of the eclipse, the peak density starts to deviate from the normal pattern between 07:30 UT and 08:00 UT, and even decreases right after the maximum of the eclipse. The solid curve represents the median behavior calculated from measurements of the 27-day period centered on the day of the eclipse.

it should be noted that the whole event happens rather quickly compared to many ionospheric processes, and that the ionosphere does not get sufficient time to reach equilibrium with this lower production rate before the eclipse has passed and the production started to increase again. This suggests that, perhaps, the topside ionosphere was not accurately modeled by LIEDR because the normal, equilibrium day-time option was used throughout. A topside profiler, that is more suitable for this kind of (non-equilibrium) conditions, would produce more accurate results; however, the finding (construction) of such profiler is still an open problem (Verhulst and Stankov, 2015).

## 7. Ionospheric plasma drift and tilt

In a detour from the traditional focus on the ionospheric peak characteristics and  $TEC$ , and in search of better

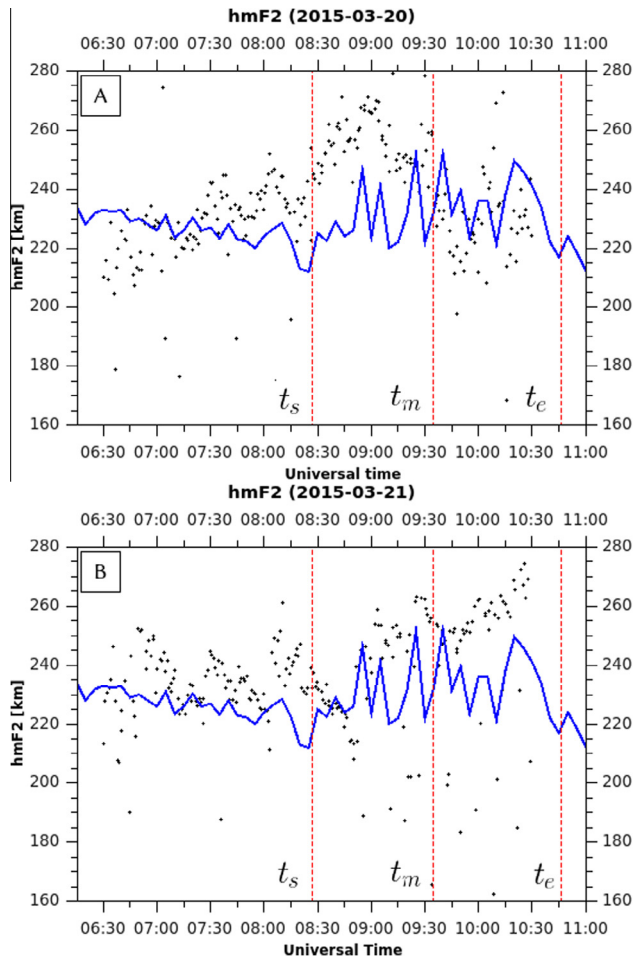


Fig. 6. Ionospheric  $F$ -layer peak height,  $h_m F_2$ , during the eclipse (panel A, crosses) and the control day (panel B, crosses). On the control day,  $h_m F_2$  exhibits the normal behavior while on the day of the eclipse, a peak appears immediately after the maximum obscuration. The solid curve represents the median behavior calculated from measurements of the 27-day period centered on the day of the eclipse.

understanding of the transport processes in the (upper) ionosphere, we carried out unprecedented ionosonde-based high-cadence plasma drift and ionospheric tilt measurements.

The Digisonde has the capability to measure the angle of arrival and Doppler shift for each received echo. Using these measurements, a SkyMap can be constructed, i.e. a two-dimensional map of the ionosphere showing the zenith and azimuth of echoes originating over a region around the ionosonde, as well as each echo's Doppler shift. The ionosonde Doppler shift is a measure of the so-called “apparent” bulk plasma drift velocity, which is a function of several time-varying properties of the radiowave propagation medium. The “apparent” velocity is normally different from the “real” velocity although there are periods and locations when they are similar or even identical. In general, the apparent velocity is a reliable measure of the plasma motion during periods of ionization equilibrium when the photoionization and recombination do not change the refractive index of the propagation medium.

The behavior of the apparent vertical plasma drift velocity ( $v_z$ ) is shown in Fig. 8. Contrary to the clear trend exhibited by  $f_o F_2$ ,  $v_z$  remains more or less the same for the entire time interval under consideration on both days. However, a few well-pronounced oscillations are detected during the eclipse (Fig. 8A). First, shortly after the start of the eclipse, at around 08:30 UT,  $v_z$  increases sharply from  $-5$  m/s up to about  $+20$  m/s and then reverses to  $-5$  m/s at 08:50 UT. This is quickly followed by a similar oscillation from  $-5$  m/s to  $+20$  m/s and back down to  $-5$  m/s ending at around 09:00 UT. Around 09:30 UT, coinciding with the maximal eclipse, again a new steep increase in  $v_z$  exceeding  $+40$  m/s is observed, followed by an equally large decrease around 10:30 UT. Note that the maximal values reached in between are unknown because they are outside the range observable by the ionosonde.

The zenith angle ( $\zeta$ ) (Fig. 9) and the azimuth angle ( $\alpha$ ) (Fig. 10) of the ionospheric tilt during the two campaign days were thoroughly investigated as well. During the observed time periods no net change in the tilt is observed. Similarly to the  $v_z$  measurements, there are some clear oscillations. Moreover, the disturbances in the tilt angles coincide with those of  $v_z$ . On the reference day, 21 March 2015, two maxima in  $\zeta$  can be seen at the same times as the  $v_z$  peaks. On the eclipse day, 20 March 2015, between 08:30 UT and 09:00 UT, there are two disturbances in the tilt, coinciding again with the peaks in  $v_z$ . But the largest fluctuation in the tilt is observed between 09:30 UT and 10:30 UT on the eclipse day, at the time of the maximal eclipse and coinciding with the large positive peak in  $v_z$ . Note that the maximum of the peak in  $\zeta$  is also outside the measurement range.

## 8. True height plasma frequency contours

Fig. 11 shows the true height contours for twelve frequencies from 2.8 MHz to 5.0 MHz respectively for the day of the eclipse (panel A) and the reference (panel B) days. These contours are derived from the traces obtained from the vertical soundings by the ARTIST-5 autoscaling software (Galkin and Reinisch, 2008). In Fig. 11A the arrows indicate wave-like disturbances similar to the oscillations seen in the drift and tilt measurements (cf. Figs. 8–10). It is important that these 3 arrow-marked variations occur concurrently in all contours together, which is usually interpreted as a sign of traveling ionospheric disturbances (TIDs) (Jakowski et al., 2008).

The advantage of high time-resolution observation is that there are multiple measurements over the course of one TID. Since the time-scale of TIDs is typically 20 to 30 min, during the usual five-minute cadency schedule there will normally only be a few measurements during a TID. This makes it more difficult to distinguish a TID among the normal variations in the scaled traces, especially when relying on auto-scaled data. TIDs are expected during eclipses, so the latter provide excellent opportunities to study TIDs with high time-resolution campaigns.

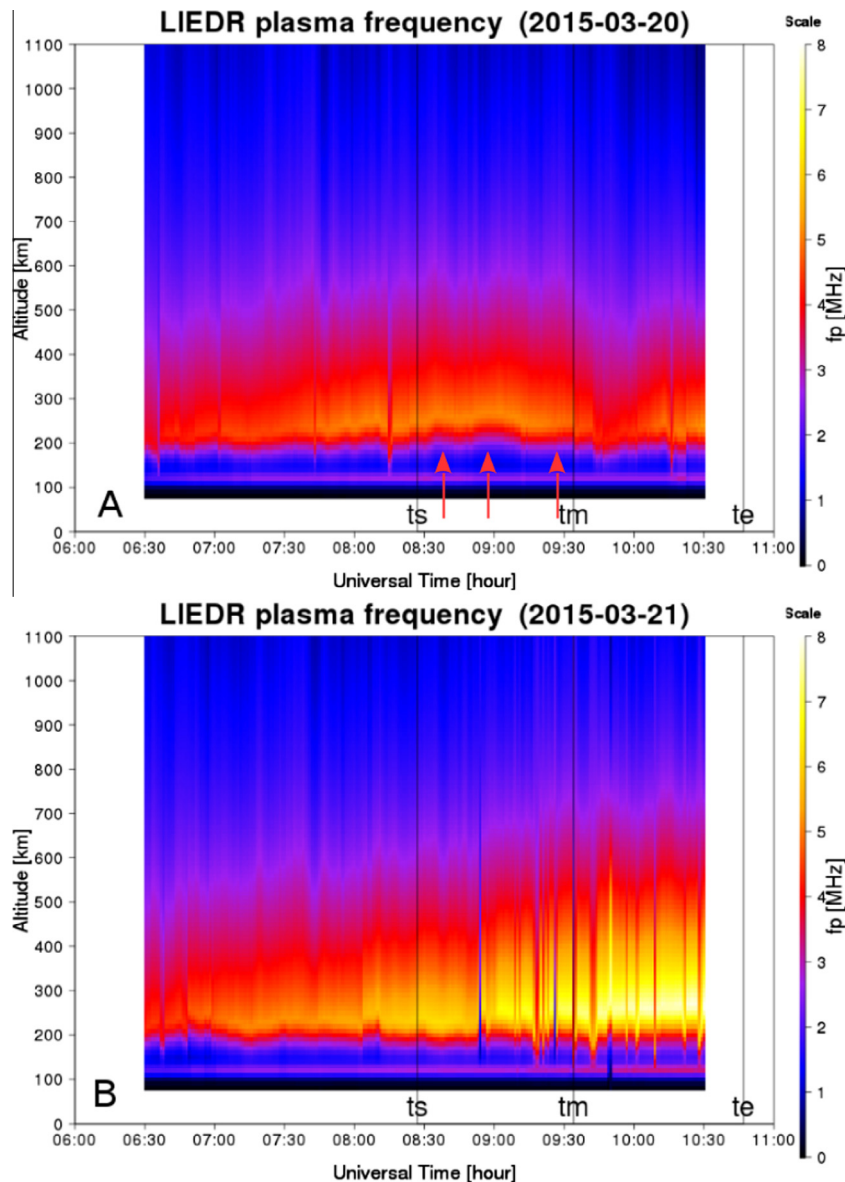


Fig. 7. Vertical electron density distribution (converted to plasma frequency in MHz), as modeled by the LIEDR system, during the eclipse (panel A) and at the same time period on the control day (panel B). The red arrows in panel A indicate the times of the most significant disturbances (cf. Fig. 11 below), believed to be related to TIDs. (For interpretation of the references to color in this figure legend, the reader is referred to the web version of this article.)

## 9. Discussion

Theoretically (Richmond, 2011), the ionospheric plasma tends to convect in the presence of an electric field as though all particles are forced to remain on a common geomagnetic-field line as they move, according to the “frozen-in” magnetic flux concept. If we adopt this concept, the plasma dynamics is then split between a field-aligned motion (which is strongly related to local processes) and a perpendicular motion (controlled by either the rotation or the convection electric field). At middle latitudes, like the location of Dourdes (50.1°N), co-rotation prevails with a slight contribution of the dawn-dusk convection electric field. The field-aligned motion is, more or

less, controlled by zonal neutral winds which have a field-aligned component. Although the ionospheric  $E$  and  $F$  regions are coupled electro-dynamically, there are substantial differences.

In the lower ionosphere ( $E$  region), photochemistry is by far the dominant process governing the plasma density and distribution. Also, the frequent collision between the ionized and neutral components in this region leads to a relatively short lifetime of the ion species, on average about one minute. As a result, the  $E$  region is expected to react much faster to any change in solar radiation. Thus, this region is a perfect proxy for eclipse monitoring, as long as it is in the shadow of the Moon. The  $f_oE$  plot (Fig. 4) clearly shows that, except during the eclipse, the  $E$  layer

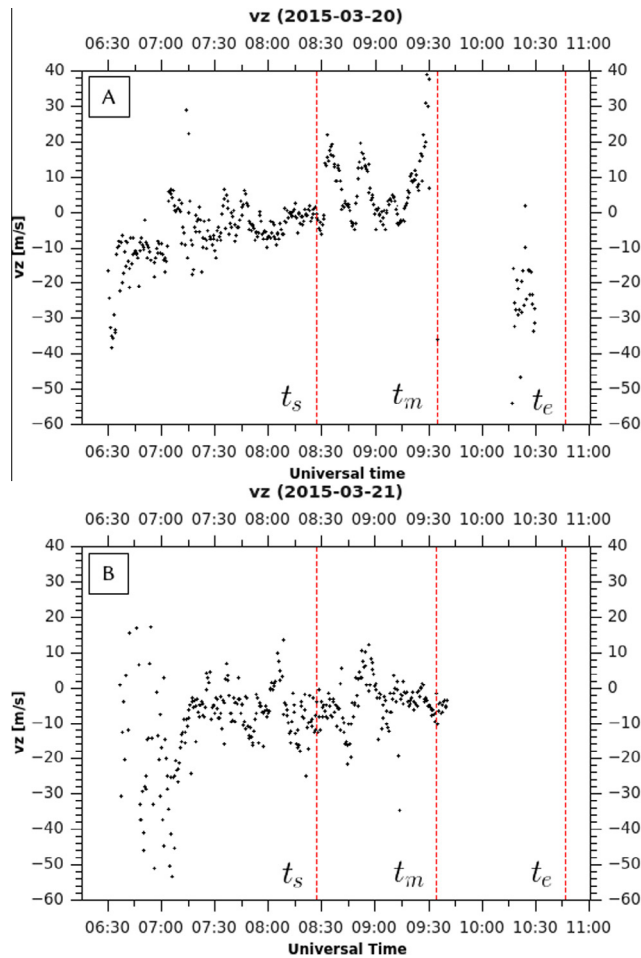


Fig. 8. Vertical component of the apparent plasma drift velocity ( $v_z$ ) during the eclipse (panel A) and the control day (panel B), positive values indicate upward direction. There is a gap in the data after the maximum obscuration due to drift values outside the instrument range.

is very similar from one day to the other, meaning that the lower ionosphere is not really affected in the period before the start of the eclipse ( $t_s$ ). Since the  $E$  region is less affected by the magnetic field, if there were some plasma transport effects prior to the eclipse to be observed, there should undoubtedly be some markers in the  $E$ -region data to be seen, which is not the case.

Something else, however, was seen in the  $E$  region during the eclipse, which needed further investigation. The  $E$ -layer critical frequency started to decrease steadily as soon as the eclipse started and reached a bottom of 2.5 MHz which remained unchanged for about 1.5 h between about 08:45 UT and 10:15 UT, including the time of the maximum eclipse. A careful inspection of the ionograms (and sky-maps) reveals that ARTIST had difficulties identifying a proper trace of the  $E$  layer and eventually offered a default daytime value of 2.5 MHz (Fig. 12A, left). The most probable explanation, in our interpretation of the data, is that the  $E$  layer was substantially depleted (almost non-existent) at around the time of the eclipse maximum, thus resembling night-time conditions. This is supported by

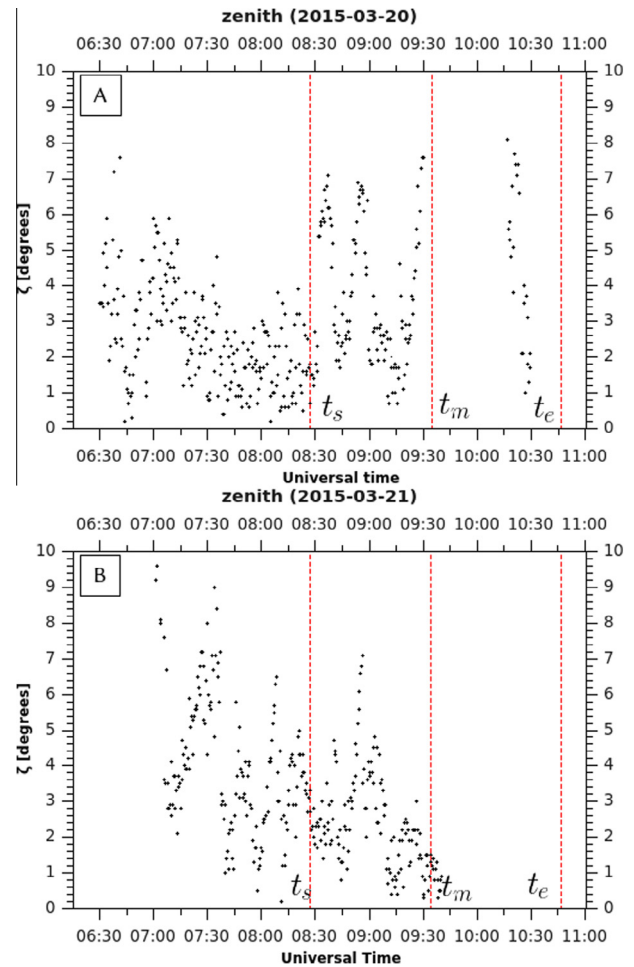


Fig. 9. Ionospheric tilt measurements—zenith angle ( $\zeta$ )—during the eclipse (A) and control (B) days. Note the data gap occurring at the same time as for the  $v_z$  data.

the substantial uplift in the true-height contours and the gap for frequencies above 4.2 MHz (Fig. 11A). Note also that simultaneous gaps occur in the drift and tilt measurements (Figs. 8–10) suggesting very large ionospheric tilt (cf. Fig. 11A, right) and drift readings (which is a sign of disturbed conditions). In fact, almost all other sky-maps around the time of the eclipse maximum ( $t_m$ ) are blank.

In the  $F$  region, the photochemistry is much less important than the transport processes. During day, near its peak density height ( $h_m F_2$ ), the  $F$  layer is, more or less, in a state of equilibrium as a result of the  $O^+$  photo production and field-aligned diffusion of this major ion in the neutral components. The characteristic time of these processes is about 20 min around a height of 200 km and increases with altitude.

As we pointed out in the previous sections, on the eclipse day, changes from the “normal” diurnal behavior of  $f_o F_2$  start to appear before the nominal start of the eclipse, and it stagnates at relatively low values for a prolonged period around the start of the eclipse over Dourbes. The recovery of both  $TEC$  and  $f_o F_2$  after the end of the

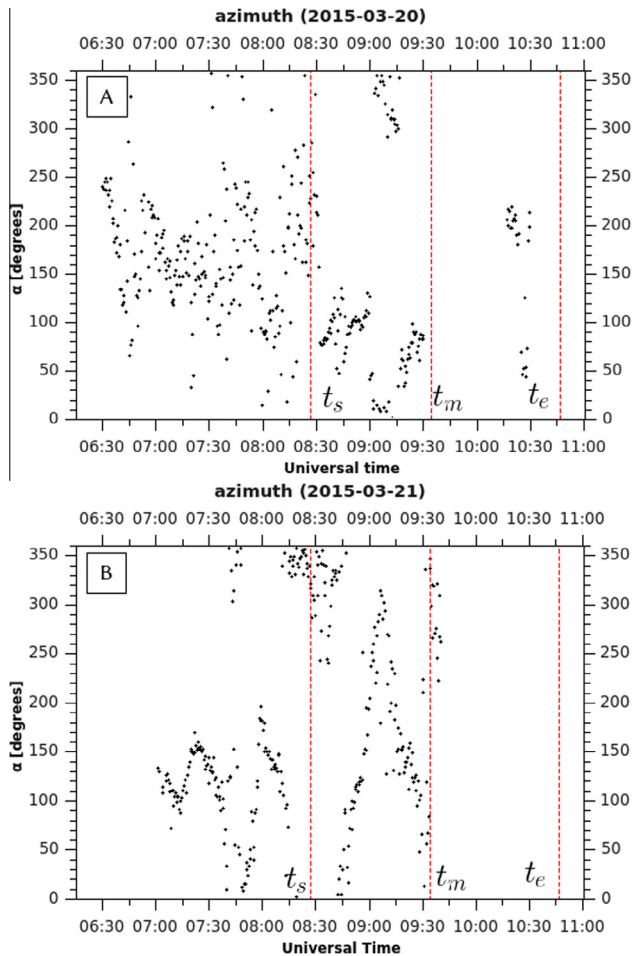


Fig. 10. Ionospheric tilt measurements—azimuth angle ( $\alpha$ )—during the eclipse (A) and control (B) days. Note the data gap occurring at the same time as the one in the  $v_z$  data.

eclipse is rather slow, and continues throughout the day. This is clearly seen in LIEDR profilograms for the two days shown in Fig. 13.

One hypothesis can be that the decrease in plasma density is due to plasma moving westward towards the region in the Atlantic where the eclipse was already in progress. However, these differences first started to appear shortly after 06:30 UT, well before the eclipse started over the ocean (07:41 UT). Since such differences are observed neither in the vertical TEC data (Fig. 3) nor in the  $h_m F_2$  data (Fig. 6), they should be associated to other processes occurring in the F region rather than being related to the eclipse. Statistically, there is not much difference between the eclipse and control day. Any differences prior to the 07:41 UT are, most probably, due to effects from the background geomagnetic conditions (Fig. 14). The eclipse occurred during the recovery phase of a strong geomagnetic storm that started a few days earlier (17 March) and the ionosphere was still depleted i.e. the plasma density was still below the mean values during the eclipse and even on the control day.

Another hypothesis that can be put forward is the field-aligned plasma transport which may affect the  $F_2$  peak density. The prolonged stagnation of  $f_o F_2$  can actually be due to a persistent plasma flux downward which would compensate the production rate. Such a flux could be due to a northward zonal neutral wind which would project along the magnetic field as a downward velocity. However, as the tilt measurements show, the echoes are not coming from straight above the ionosonde, and we cannot exclude that this may be an artifact related to the real direction probed.

The key to understanding what is going on might be found in the drift and tilt measurements. Indeed, when the eclipse reaches Dourbes, the vertical component of the drift velocity,  $v_z$  (Fig. 8), increases sharply from a low negative value ( $-5$  m/s) to a high positive value ( $+20$  m/s) and then decreases again to the negative value of about  $-5$  m/s. At the same time, the zenith angle (Fig. 9) increases from  $1-2^\circ$  up to  $7^\circ$ , then back down to  $2^\circ$ , while the azimuth (Fig. 10) changes from Northwest to Southeast then back to Northwest. The first oscillation of the vertical drift velocity and the zenith angle seems to be related to the beginning of the eclipse when the ionosonde switches from a westward pointing direction to an eastward direction. The second oscillation occurs on both the eclipse and control days at the same time. On the control day, the azimuth sweeps  $720^\circ$  in one hour while, on the eclipse day, the pointing direction is North to East. This can be interpreted as a result of an inhomogeneous ionosphere. The third oscillation is clearly associated to the maximum of the eclipse, when a large area around the sounder is in the shadow of the Moon. The ionosonde is then pointing eastward (South-East), i.e. towards regions which are not yet or, at least, less affected by the eclipse. The apparent vertical velocity seems to be related to an increasing zenith angle towards East. It seems that the ionosonde is following the edge of the shadow. If this is correct, then the vertical drift velocity can be considered as an estimate of the line-of-sight velocity of the shadow of the moon. At the maximum of the eclipse, it is pointing eastward (azimuth about  $80^\circ$ ) with an apparent velocity exceeding  $+40$  m/s. This represents, at altitudes near the  $F_2$  peak, a distance of about  $+40$  km eastwards and a substantial horizontal velocity of about  $700$  m/s.

The oscillations observed in the drift and tilt measurements (Figs. 8–10) coincide precisely in time with the simultaneous wave-like variations in all of the trueheight curves (Fig. 11). Moreover, the wave patterns in the bottomside ionosphere are clearly seen in the model reconstruction by LIEDR (Fig. 7), including obvious effects on the topside ionospheric plasma re-distribution. The characteristics and the similarities between these wave-like patterns, observed via different measurements, suggest a manifestation of TIDs. One credible explanation is a bow-wave-like disturbance in the neutral atmosphere, produced by the shadow of the moon. However, more high-resolution

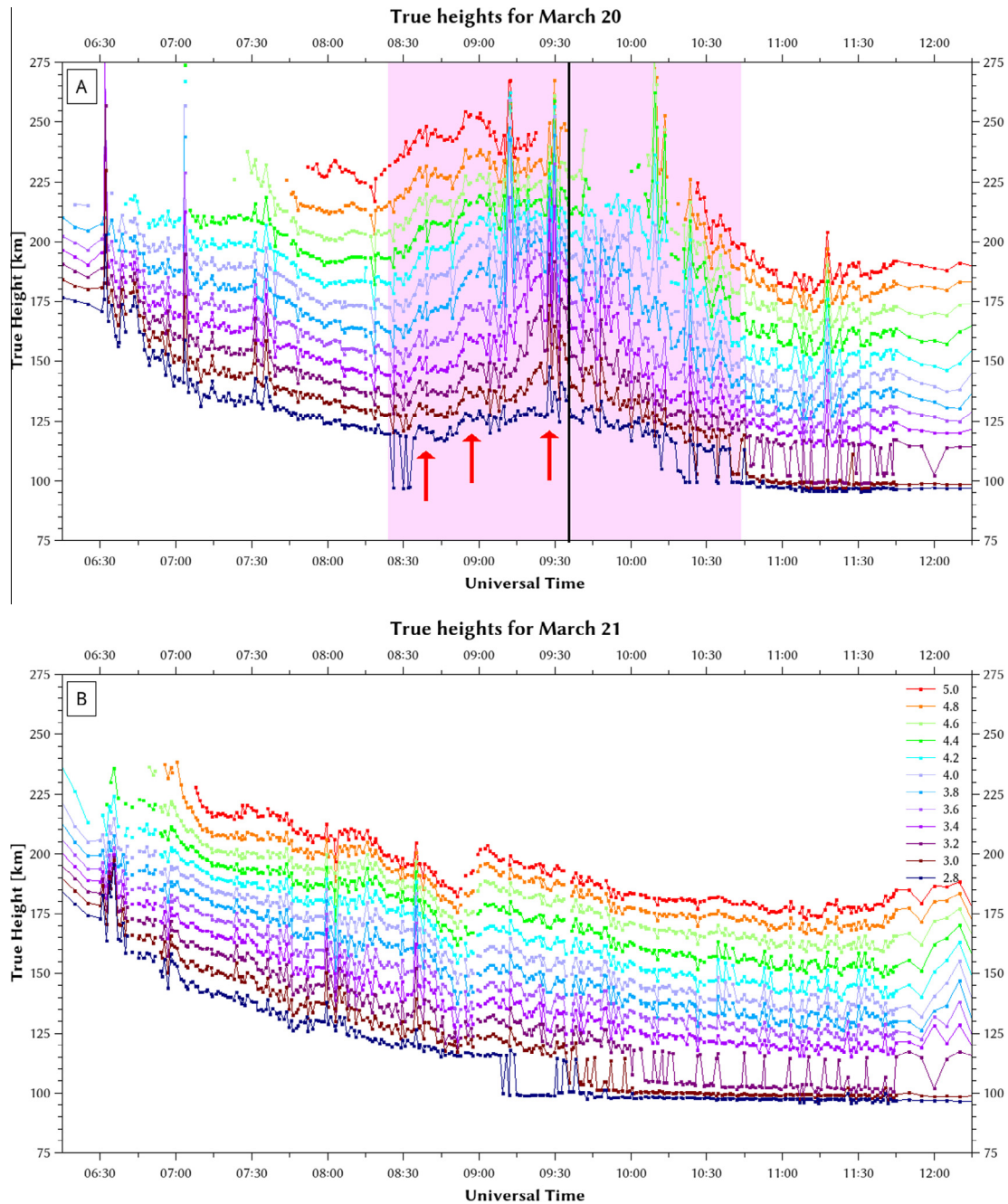


Fig. 11. True-height contours for the eclipse day, 20 March (panel A), and the control day, 21 March (panel B), as derived by the ARTIST-5 software. Frequencies range from 2.8 MHz to 5.0 MHz, in steps of 0.2 MHz. The shading covers the period of the eclipse and the vertical black line indicates the moment of maximal eclipse. The red arrows point at the times of the oscillation peaks observed in the drift and tilt measurements (cf. Figs. 8–10). Each dot corresponds to a separate sounding. It can also be seen on these plots that the lowest frequencies start falling below  $f_oE$  from around 10:15 UT on 20 March (A) and around 09:10 UT on 21 March (B). (For interpretation of the references to color in this figure legend, the reader is referred to the web version of this article.)

data from various sources (in situ measurements, incoherent scatter radar, ionosonde, etc.) and multiple events is needed to form a clear picture of the generation and propagation of TIDs produced by eclipses.

Last but not least, when interpreting local eclipse effects, it should be taken into account that the response of the ionosphere to an eclipse can be very different depending

on location (eclipse path), local time and season. For example, during eclipse occurring at low latitudes (Madhav Haridas and Manju, 2012), an increase in  $f_oF_2$  might be observed instead of a decrease. Of course, at high latitudes (Rashid et al., 2006), a different type of behavior of some (or all) of these ionospheric characteristics should not be excluded.



## 10. Conclusion

During the eclipse, the behavior of the ionospheric *F* layer characteristics and the *TEC* was as expected for this time of day and season, and is in agreement with previous eclipse studies. The observations of drift and tilt during an eclipse, especially at this time resolution, are unprecedented. The most remarkable feature is the close correlation between the zenith angle and the vertical plasma velocity. This is particularly true for the TIDs caused by the eclipse, which can be observed in both tilt and drift measurements as well as in the true-height contours obtained from vertical soundings.

## Acknowledgments

This study is funded by the Royal Meteorological Institute (RMI) via the Belgian Solar-Terrestrial Centre of Excellence (STCE). The solar radio data used here come from the Humain Radio Astronomy Station where solar monitoring instruments are operated by the Royal Observatory of Belgium (ROB) in the framework of STCE. We thank Dr. Christophe Marqué (ROB) for the helpful discussions and SRF data.

## References

- Afraimovich, E.L., Palamartchouk, K.S., Perevalova, N.P., Chernukhov, V.V., Likhnev, A.V., Zalutsky, V.T., 1998. Ionospheric effects of the solar eclipse of March 9, 1997, as deduced from GPS data. *Geophys. Res. Lett.* 25 (4), 465–468. <http://dx.doi.org/10.1029/98GL00186>.
- Altadill, D., Sole, J.G., Apostolov, E.M., 2001. Vertical structure of a gravity wave like oscillation in the ionosphere generated by the solar eclipse of August 11, 1999. *J. Geophys. Res.* 106 (A10), 21419–21428. <http://dx.doi.org/10.1029/2001JA900069>.
- Bamford, R.A., 2001. The effect of the 1999 total solar eclipse on the ionosphere. *Phys. Chem. Earth (C)* 26 (5), 373–377. [http://dx.doi.org/10.1016/S1464-1917\(01\)00016-2](http://dx.doi.org/10.1016/S1464-1917(01)00016-2).
- Baron, M.J., Hunsucker, R.D., 1973. Incoherent scatter radar observations of the auroral zone ionosphere during the total solar eclipse of July 10, 1972. *J. Geophys. Res.* 78, 7451–7460. <http://dx.doi.org/10.1029/JA078i031p07451>.
- Beynon, W.J.G., Brown, G.M. (Eds.), 1956. *Solar Eclipses and the Ionosphere*. Pergamon Press, London.
- Chimonas, G., Hines, C.O., 1970. Atmospheric gravity waves induced by a solar eclipse. *J. Geophys. Res.* 75 (4), 857–875. <http://dx.doi.org/10.1029/JA075i004p00875>.
- Chuo, Y.J., 2013. Ionospheric effects on the F region during the sunrise for the annular solar eclipse over Taiwan on 21 May 2012. *Ann. Geophys.* 31 (11), 1891–1898. <http://dx.doi.org/10.5194/angeo-31-1891-2013>.
- Davis, C.J., Clarke, E.M., Bamford, R.A., Lockwood, M., Bell, S.A., 2001. Long term changes in EUV and X-ray emissions from the solar corona and chromosphere as measured by the response of the Earth's ionosphere during total solar eclipses from 1932 to 1999. *Ann. Geophys.* 19 (3), 263–273. <http://dx.doi.org/10.5194/angeo-19-263-2001>.
- Farges, T., Jodogne, J.C., Bamford, R., Le Roux, Y., Gauthier, F., Vila, P.M., Altadill, D., Sole, J.G., Miro, G., 2001. Disturbances of the western European ionosphere during the total solar eclipse of 11 August 1999 measured by a wide ionosonde and radar network. *J. Atmos. Sol.-Terr. Phys.* 63 (9), 915–924. [http://dx.doi.org/10.1016/S1364-6826\(00\)00195-4](http://dx.doi.org/10.1016/S1364-6826(00)00195-4).
- Galkin, I.A., Reinisch, B.W., 2008. The new ARTIST-5 for all digisondes. *Ionosonde Network Advisory Group (INAG) Bull.* 69, 1–8.
- Jakowski, N., Stankov, S.M., Wilken, V., Borries, C., Altadill, D., Chum, J., Buresova, D., Sauli, P., Hruska, F., Cander, L.J.R., 2008. Ionospheric behavior over Europe during the solar eclipse of 3 October 2005. *J. Atmos. Sol.-Terr. Phys.* 70 (6), 836–853. <http://dx.doi.org/10.1016/j.jastp.2007.02.016>.
- Klobuchar, J.A., Whitney, H.E., 1965. Ionospheric electron content measurements during a solar eclipse. *J. Geophys. Res.* 70 (5), 1254–1257. <http://dx.doi.org/10.1029/JZ070i005p01254>.
- Korenkov, Y.N., Klimenko, V.V., Bessarab, F.S., Nutsvalyan, N.S., Stanislawski, I., 2002. Model/data comparison of the F2-region parameters for the 11 August 1999 solar eclipse. *Adv. Space Res.* 31 (4), 995–1000. [http://dx.doi.org/10.1016/S0273-1177\(02\)00816-5](http://dx.doi.org/10.1016/S0273-1177(02)00816-5).
- Kozlov, A.V., Paznukhov, V.V., 2008. Digisonde digisonde drift analysis software. *AIP Conf. Proc.* 974, 167–174.
- Kumar, S., Singh, A.K., Singh, R.P., 2013. Ionospheric response to total solar eclipse of 22 July 2009 in different Indian regions. *Ann. Geophys.* 31 (9), 1549–1558. <http://dx.doi.org/10.5194/angeo-31-1549-2013>.
- Le, H., Liu, L., Yue, X., Wan, W., Ning, B., 2009. Latitudinal dependence of the ionospheric response to solar eclipse. *J. Geophys. Res.* 114 (A7), A07308. <http://dx.doi.org/10.1029/2009JA014072>.
- Madhav Haridas, M.K., Manju, G., 2012. On the response of the ionospheric F region over Indian low-latitude station Gadanki to the annular solar eclipse of 15 January 2010. *J. Geophys. Res.* 117, A01302. <http://dx.doi.org/10.1029/2011JA016695>.
- Müller-Wodarg, I.C.F., Aylward, A.D., Lockwood, M., 1998. Effects of a mid-latitude solar eclipse on the thermosphere and ionosphere – a modelling study. *Geophys. Res. Lett.* 25 (20), 3787–3790. <http://dx.doi.org/10.1029/1998GL900045>.
- Nestorov, G., Taubenheim, J., 1962. Untersuchungen an der ionosphärischen E-Schicht während der totalen Sonnenfinsternis 15 February 1961. *J. Atmos. Terr. Phys.* 24 (7), 633–642. [http://dx.doi.org/10.1016/0021-9169\(62\)90085-5](http://dx.doi.org/10.1016/0021-9169(62)90085-5).
- Rashid, Z.A.A., Momani, M.A., Sulaiman, S., Ali, M.A.M., Yatim, B., Fraser, G., Sato, N., 2006. GPS ionospheric TEC measurement during the 23rd November 2003 total solar eclipse at Scott base Antarctica. *J. Atmos. Sol.-Terr. Phys.* 68 (11), 1219–1236. <http://dx.doi.org/10.1016/j.jastp.2006.03.006>.
- Reinisch, B.W., Galkin, I.A., Khmyrov, G.M., 2009. New digisonde for research and monitoring applications. *Radio Sci.* 44 (1), RS0A24. <http://dx.doi.org/10.1029/2008RS004115>.
- Richmond, A.D., 2011. Electrodynamic of ionosphere–thermosphere coupling. In: Abdu, M.A., Pancheva, D. (Eds.), *Aeronomy of the Earth's Atmosphere and Ionosphere*. Springer, The Netherlands, pp. 191–201. [http://dx.doi.org/10.1007/978-94-007-0326-1\\_13](http://dx.doi.org/10.1007/978-94-007-0326-1_13).
- Rishbeth, H., 1968. Solar eclipses and ionospheric theory. *Space Sci. Rev.* 8, 543–554. <http://dx.doi.org/10.1007/BF00175006>.
- Rishbeth, H., 1970. Eclipse effects in the ionosphere. *Nature* 226 (5251), 1099–1100. <http://dx.doi.org/10.1038/2261099a0>.
- Stankov, S.M., 2002. Reconstruction of the upper electron density profile from the over-satellite electron content. *C.R. Acad. Bulg. Sci.* 55 (2), 31–36.
- Stankov, S.M., Muhtarov, P.Y., 2001. Reconstruction of the electron density profile from the total electron content using upper transition level and vertical incidence sounding measurements. *C.R. Acad. Bulg. Sci.* 54 (9), 45–48.
- Stankov, S.M., Jakowski, N., Heise, S., Muhtarov, P., Kutiev, I., Warnant, R., 2003. A new method for reconstruction of the vertical electron density distribution in the upper ionosphere and plasmasphere. *J. Geophys. Res.* 108 (A5), 1164. <http://dx.doi.org/10.1029/2002JA009570>.
- Stankov, S.M., Stegen, K., Muhtarov, P., Warnant, R., 2011. Local ionospheric electron density profile reconstruction in real time from simultaneous ground-based GNSS and ionosonde measurements. *Adv. Space Res.* 47 (7), 1172–1180. <http://dx.doi.org/10.1016/j.asr.2010.11.039>.

- Stankov, S.M., Jodogne, J.C., Kutiev, I., Stegen, K., Warnant, R., 2012. Evaluation of automatic ionogram scaling for use in real-time ionospheric density profile specification: dourbes DGS-256/ARTIST-4 performance. *Ann. Geophys.* 55 (2), 283–291. <http://dx.doi.org/10.4401/ag-4976>.
- Verhulst, T., Stankov, S.M., 2015. Ionospheric specification with analytical profilers: evidences of non-Chapman electron density distribution in the upper ionosphere. *Adv. Space Res.* 55 (8), 2058–2069. <http://dx.doi.org/10.1016/j.asr.2014.10.017>.